Methods

Laboratory measurements of seismic velocities (Christensen, 1996) were corrected using a geothermal gradient of 10 ˚C km^{-1}. This geothermal gradient is less that measured in Taiwan (Wu et al., 2013), but is in keeping with that determined from prograde metamorphic pressure-temperature paths of high-pressure rocks worldwide (Erdman and Lee, 2014; Agard et al., 2009; Maruyama et al., 1996). Velocities were also corrected for effective pressure using the equation Pe = Pc-nPf (Christensen, 1989; Todd and Simmons, 1972). Pc is lithostatic pressure, which was calculated using a density of 2.85 g/cm^3; n is the effective-pressure coefficient, which is calculated a each depth interval using the equation of Todd and Simmons (1972). In this equation a constant differential pressure (Pd) is set to 0.005 Mpa and a constant fluid pressure (Pp) is to 0.1 Mpa. Pf is fluid pressure and, in this paper, a value for □ (Pf/Pc) is set to 0.75. The database of laboratory velocity measurements does not contain measurements of Vp and Vs for harzburgite, lherzolite, and blueschist. These were calculated using the Excel macro PhysProps (Hacker and Abers, 2003). For these calculations, mineral modal abundance and chemical data for more than 40 samples for each rock type were taken from the literature (except the Taiwan blueschist, where only 4 samples with sufficient information have been published). Vp and Vs were then calculated at STP and subsequently corrected for temperature using the same thermal coefficients as for the laboratory measurements (Christensen, 1996). The velocity effect of serpentine on mantle rock types was calculated from a best fit linear regression of published Vp and Vs data of variably serpentinized peridiotite (Christensen, 1966), combined with a larger data set determined using PhysProps at the same temperature and pressure for those reported from the laboratory measurements; 20 ˚C and 1 GPa.

All hypocenters have been relocated using the double-difference location technique and have been projected on to the velocity sections from 9.99 km either side. Focal mechanisms were determined for 57 events larger than M_L 3 and a quality value (Wu et al., 2008) greater than 1. Of these, 10 events with $M_L > 3.9$ were decomposed into double-couple and compensated linear vector dipole components. These ten events were taken from Broadband Array in Taiwan for Seismology database and the instrument response deconvolved, integrating the seismograms from ground velocity to ground displacement, and rotating the horizontal components to the radial and transverse direction for each station. A band-pass filter for frequencies between 0.03 and 0.08 Hz was applied to the data using a fourth-order minimum-phase (causal) Butterworth filter. Different weightings are assigned in the inversion according to the quality (signal-to-noise ratio) of the observed waveforms. We use an inversion algorithm (Kikuchi and Kanamori, 1991) that decomposes the moment tensor into five double-couples (pure strike-slip faults, dip-slip faults on vertical planes striking N-S and E-W, and 45° dip-slip faults) and an explosive source. In this way, the full moment tensor is represented by a linear combination of six elementary moment tensors. Here, the synthetics are formed using Green's functions computed with a numerical implementation of the propagator-matrix approach based on the 1-D layer model, which is used by the Central Weather Bureau for locating regional earthquakes, and then filtered between 0.03 and 0.08 Hz. Due to uncertainty in the event location and assumed velocity model, the synthetic waveforms do not perfectly align with the observed seismograms. Therefore, the data and synthetics waveforms are cross-correlated and the observed seismograms are shifted to maximize the cross-correlation coefficients, with an allowance of ±2 s time shifts. The adjustment is done for each component individually. Finally, the moment tensor solution is determined in a least squares sense, and the fit quantified using both variance reduction and normalized cross-correlation coefficient.

References

Agard, P., Yamato, P., Jolivert, L. and Burov, E., 2009, Exhumation of oceanic blueschists and eclogites in subduction zones: Timing and mechanisms, Earth Science Reviews, v. 92, 53-79.

Christensen, N.I., 1966, Elasticity of ultrabasic rocks. Journal of Geophysical Research, v. 71, 5921-5931.

Christensen, N.I. 1989, Pore pressure, seismic velocities, and crustal structure. in, Pakiser, L.C. and Mooney, W.D., Geophysical framework of the continental United States. Geological Society of America Memoir 172, 783-798.

Christensen, N.I., 1996, Poisson's ratio and crustal seismology. Journal of Geophysical Research, v. 101, 3139-3156.

Erdman, M.E and Lee, C.-Y. A., 2014, Oceanic- and continental-type metamorphic terranes: Occurrence and exhumation mechanisms, Earth Science Reviews, v. 139, 33-46.

Hacker, B.R. & Abers, G.A., 2003, Subduction factory 3: An Excel worksheet and macro for calculating the densities, seismic wave speeds, and H_2O contents of minerals and rocks at pressure and temperature, Geochemistry, Geophysics, Geosystems, v. 5, doi:10.1029/2003GC000614.

Kikuchi, M. & Kanamori, H., 1991, Inversion of complex body waves-III. Bulletin of the Seismological Society of America, v. 81, 2335-2350.

Maruyama, S., Liou, J.G. and Terabayashi, M., 1996, Blueschists and eclogites of the world and their exhumation, International Geology Review, v. 38, 485-594.

Todd, T. and Simmons, G., 1972, Effect of pore pressure on the velocity of compressional waves in low-porosity rocks, Journal of Geophysical Research, 77, 3731-3743.

Wu, S.-K, Chi, W.-C., Hsu, S.-M., Ke, C.-C. and Wang, Y., 2013, Shallow crustal thermal structures of central Taiwan foothills region, Terrestrial Atmospheric and Oceanic Sciences, v. 24, 695-707.

Wu, Y.-M., Zhao, L., Chang, C.-H. and Hsu, Y.-J., 2008, Focal-mechanism determination in Taiwan by genetic algorithm, Bulletin of the Seismological Society of America, v. 98, 651-661.

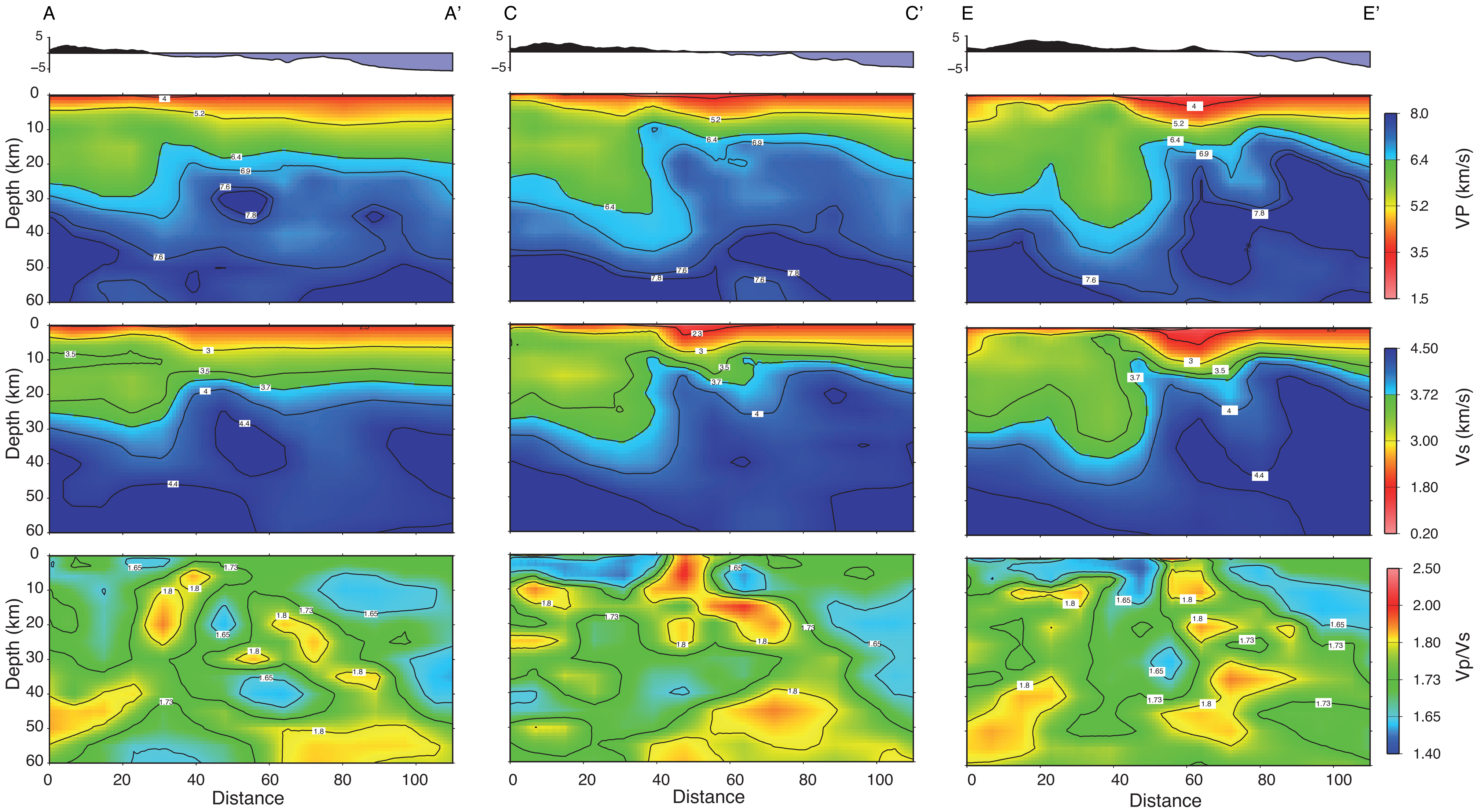

Figure S1. Tomography sections of Vp, Vs, and Vp/Vs across eastern Taiwan. The locations are shown in Figure 1.

Rock name	Symbol
Andesite	AND
Basalt	BAS
Diabase	DIA
Granite-granodiorite	GRA
Diorite	DIO
Gabbro-Norite	GAB
Greenschist basalt	BGR
Biotite(tonalite) gneiss	BGN
Mica quartz schist	QSC
Amphibolite	AMP
Felsic granulite	FSG
Paragranulite	PGR
Mafic garnet granulite	GGR
Mafic eclogite	ECL
Serpentinite	SER
Calcite marble	MBL
Hornblendite	HBL
Pyroxenite	PYX
Dunite	DUN
Harzburgite	HRZ
Lherzolite	LRZ
Blueschist	BLU
Taiwan blueschist	TWN

Figure S2. Rock name and labels for the plots in Figure 3 and the 33 different rocks types shown here, as well as the plots at 10 kilometer depth intervals. The Vp, Vs, and Vp/Vs range of interest at each depth interval is indicated by the black cross.

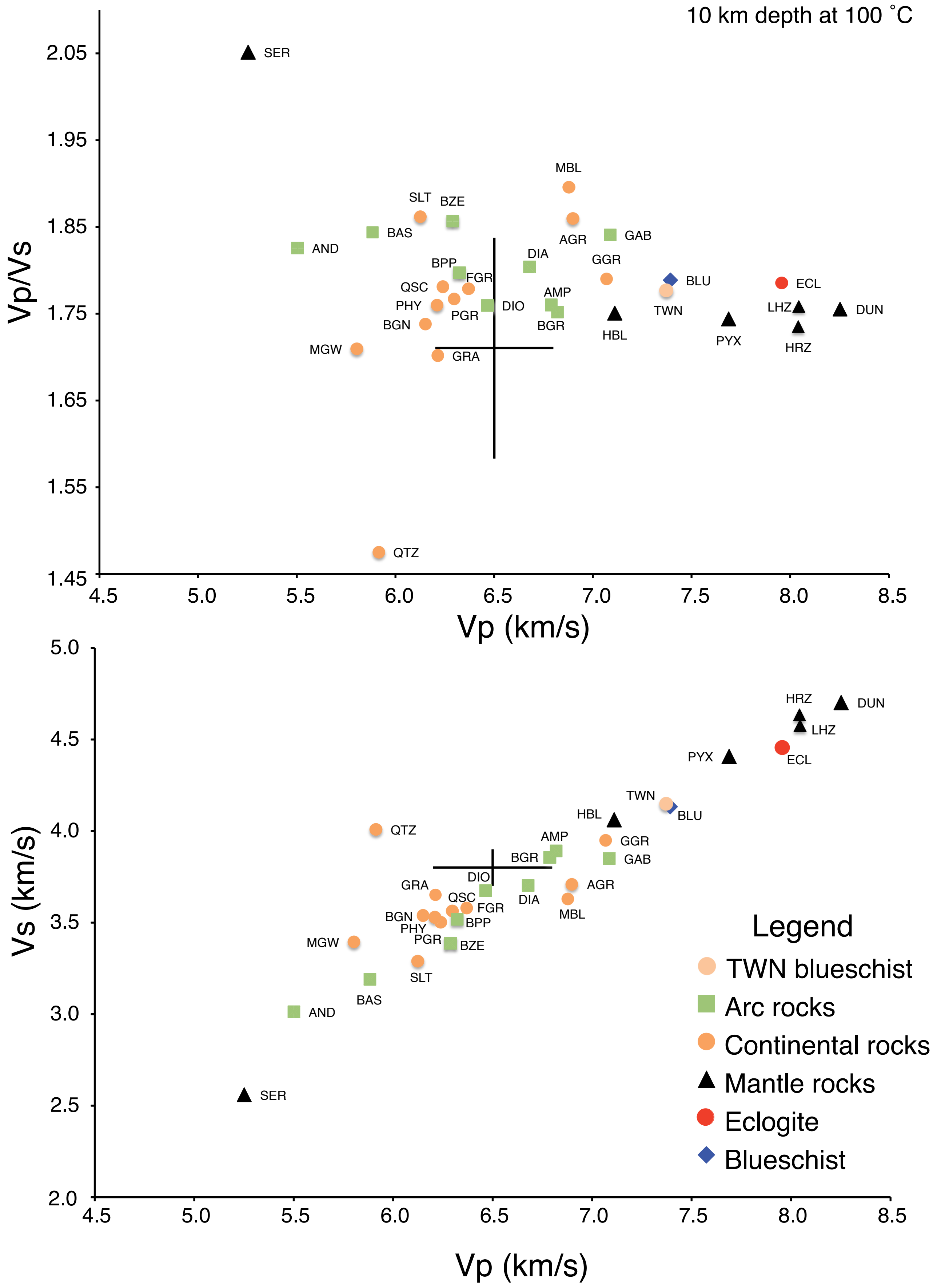

Figure S2. continued. Plots at 10 kilometer depth intervals. The Vp, Vs, and Vp/Vs range of interest at each depth interval is indicated by the black cross.

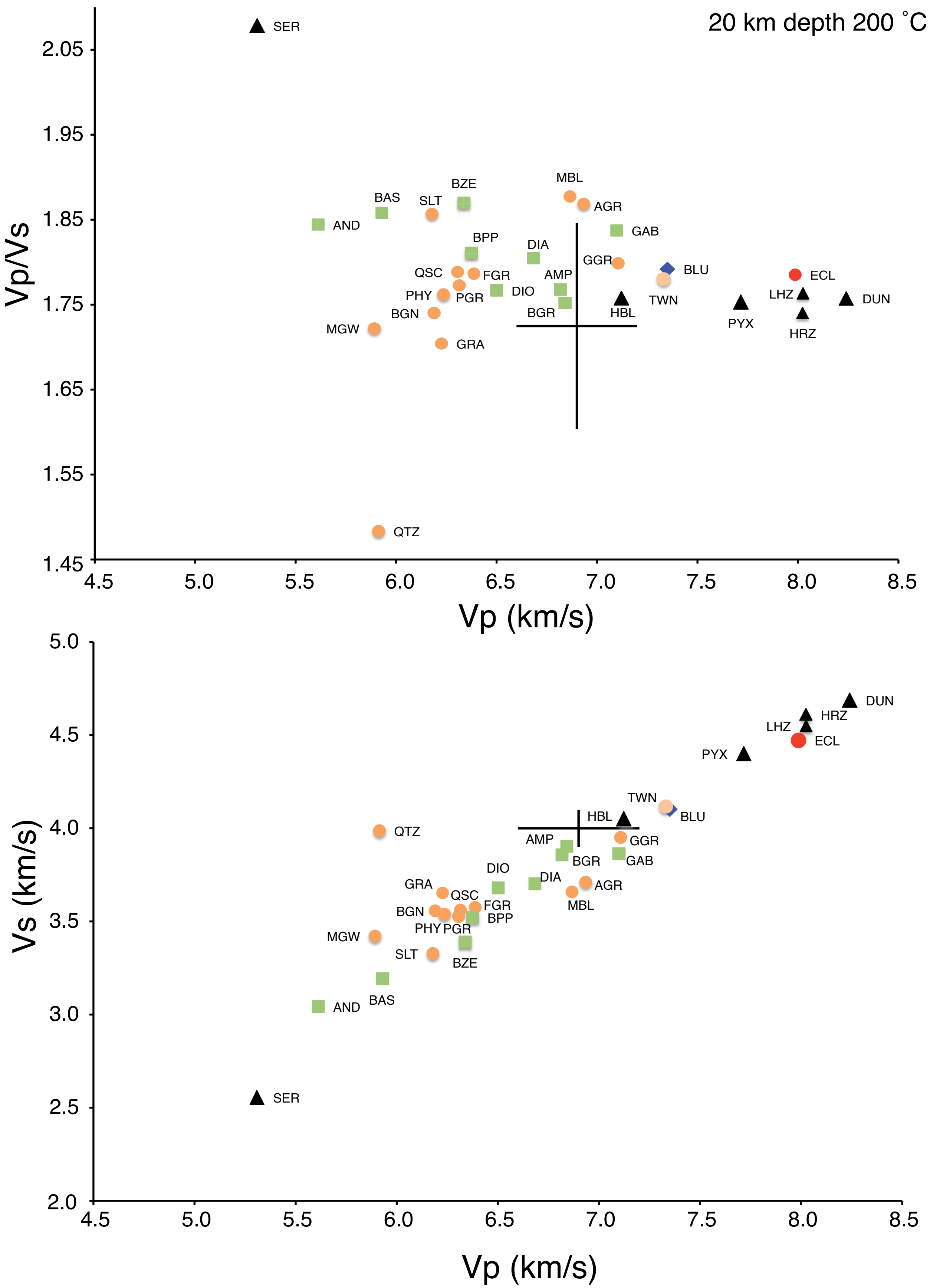

Figure S2. continued. Plots at 10 kilometer depth intervals. The Vp, Vs, and Vp/Vs range of interest at each depth interval is indicated by the black cross.

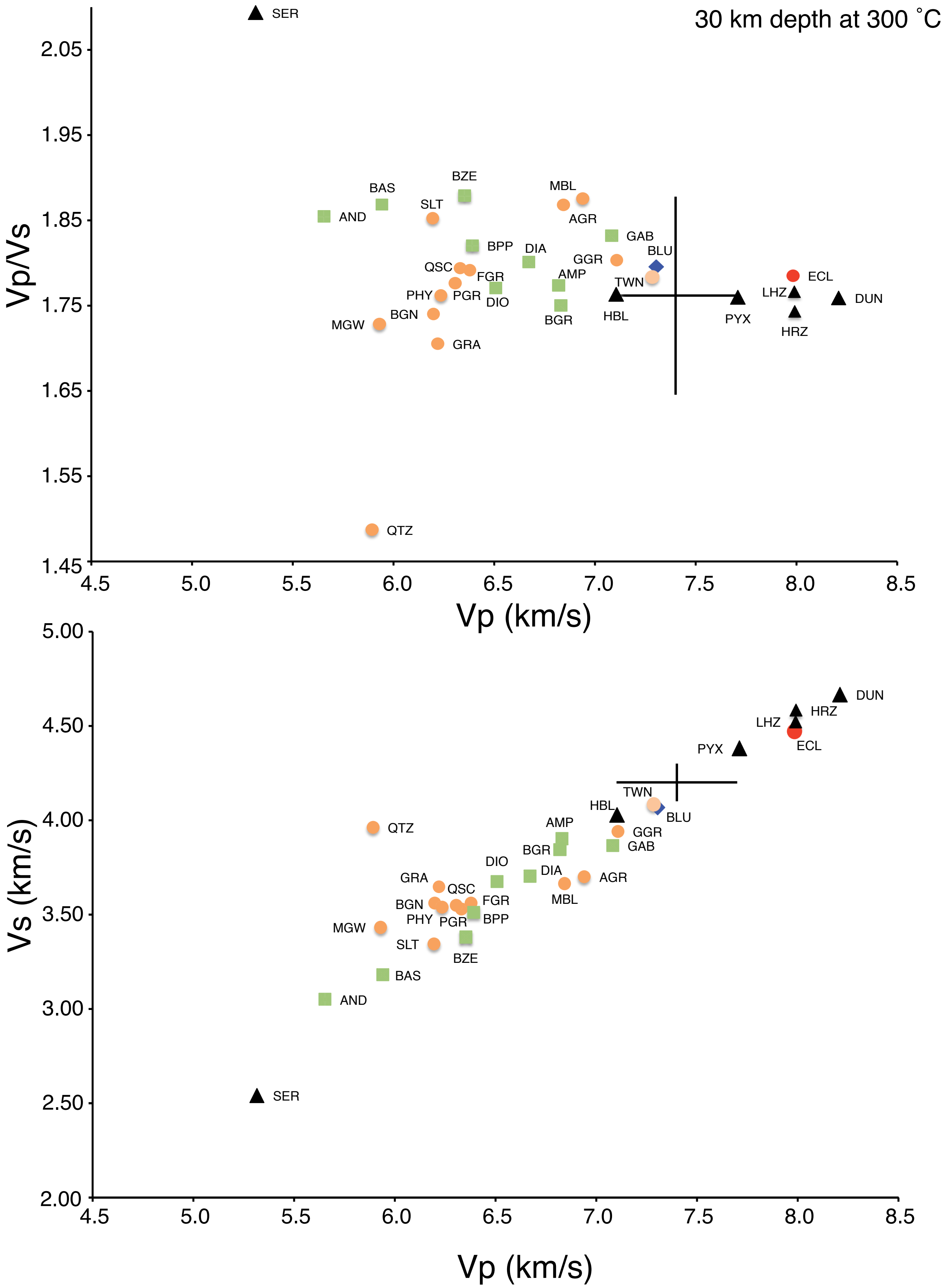

Figure S2. continued. Plots at 10 kilometer depth intervals. The Vp, Vs, and Vp/Vs range of interest at each depth interval is indicated by the black cross.

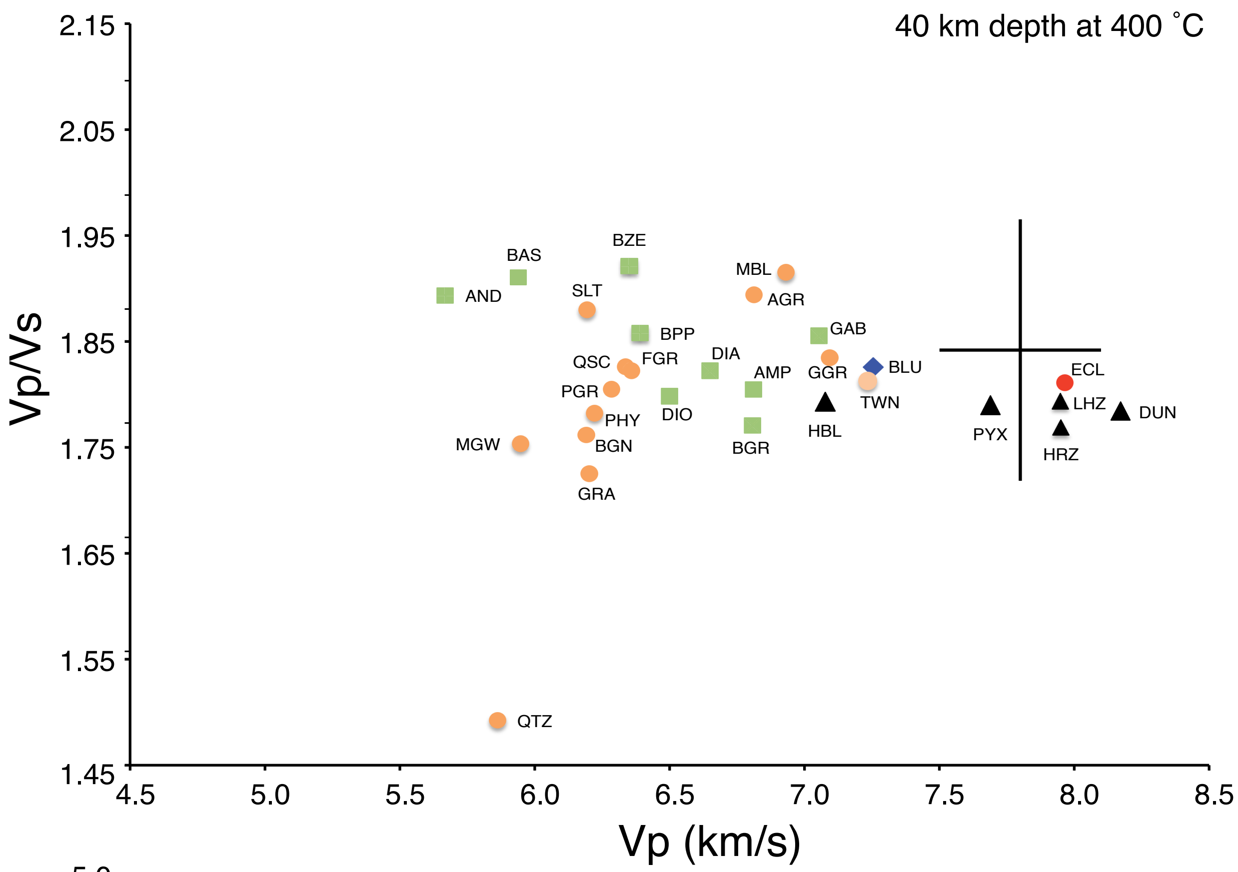

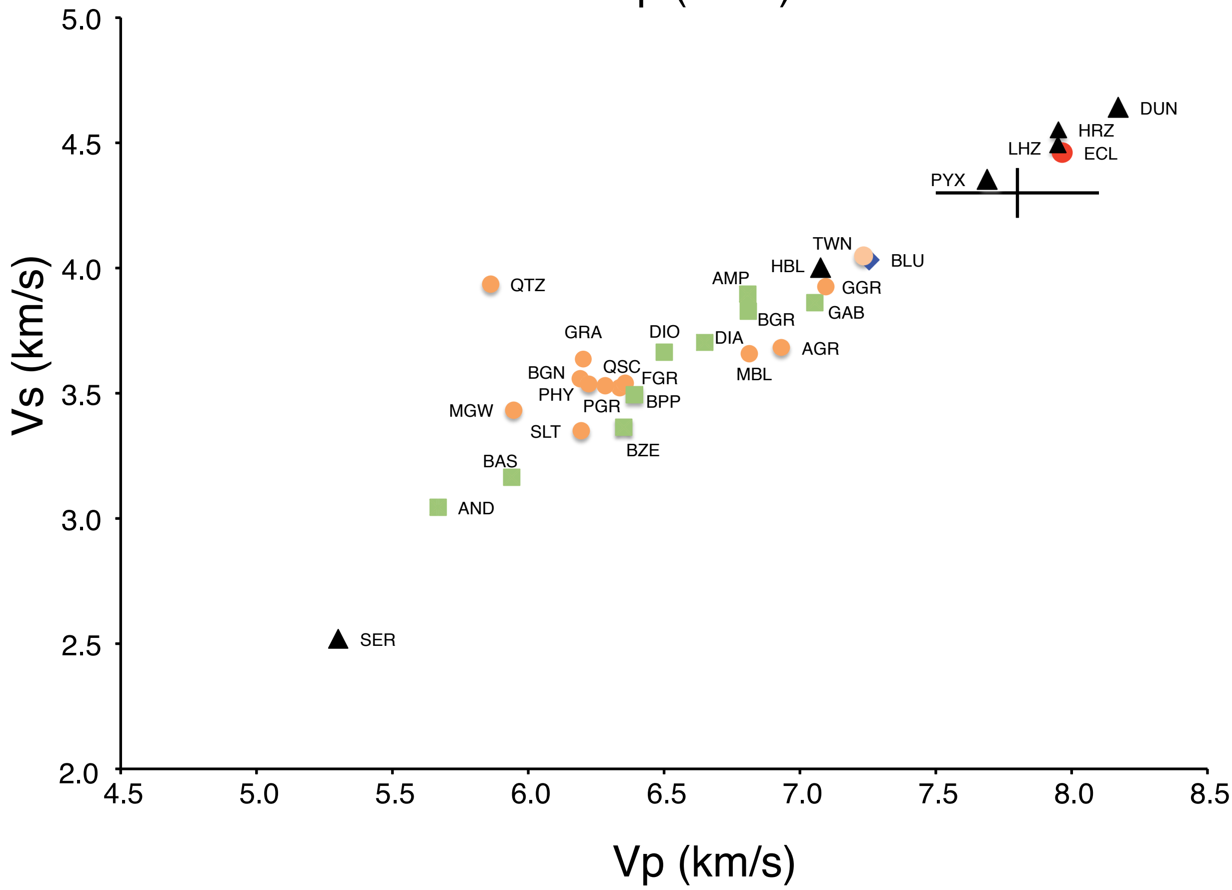

Figure S2. continued. Plots at 10 kilometer depth intervals. The Vp, Vs, and Vp/Vs range of interest at each depth interval is indicated by the black cross.

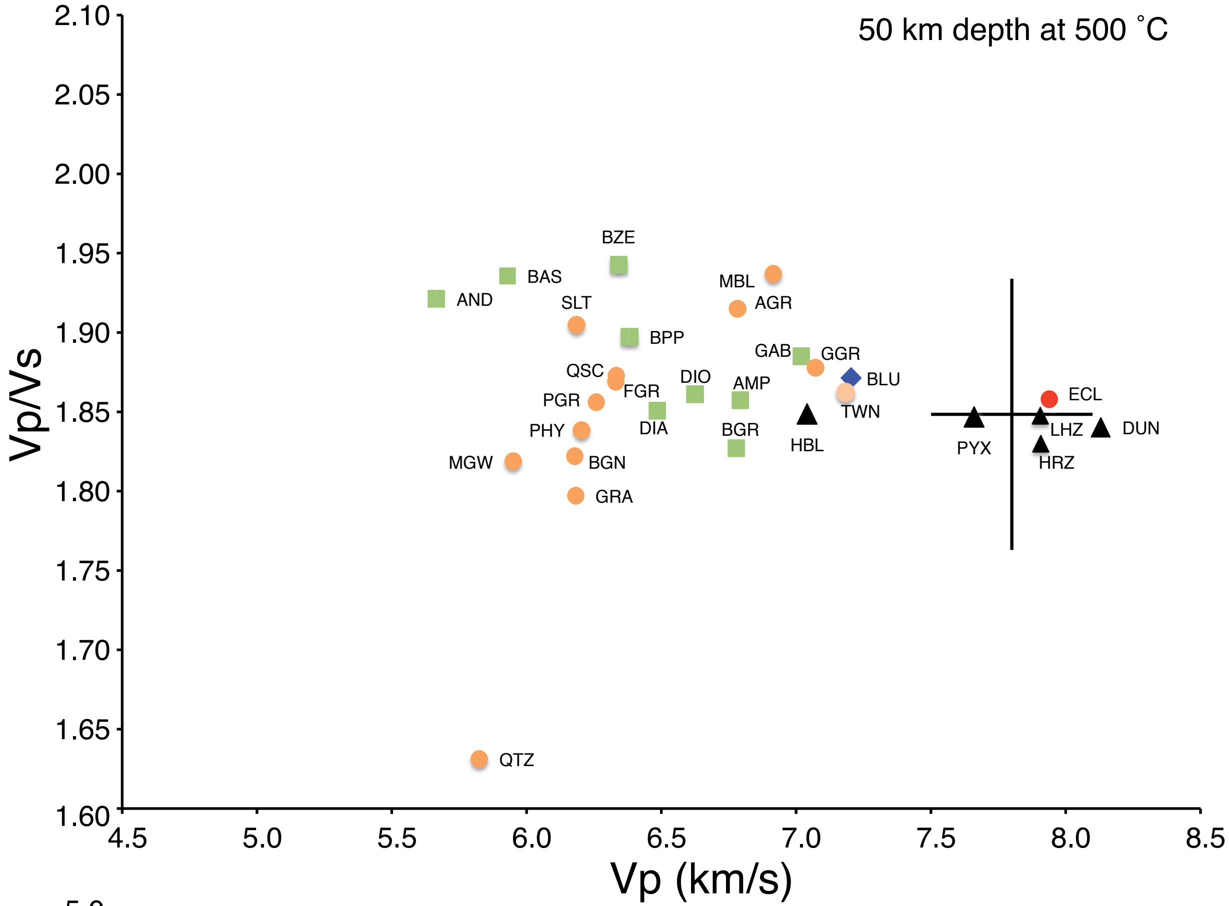

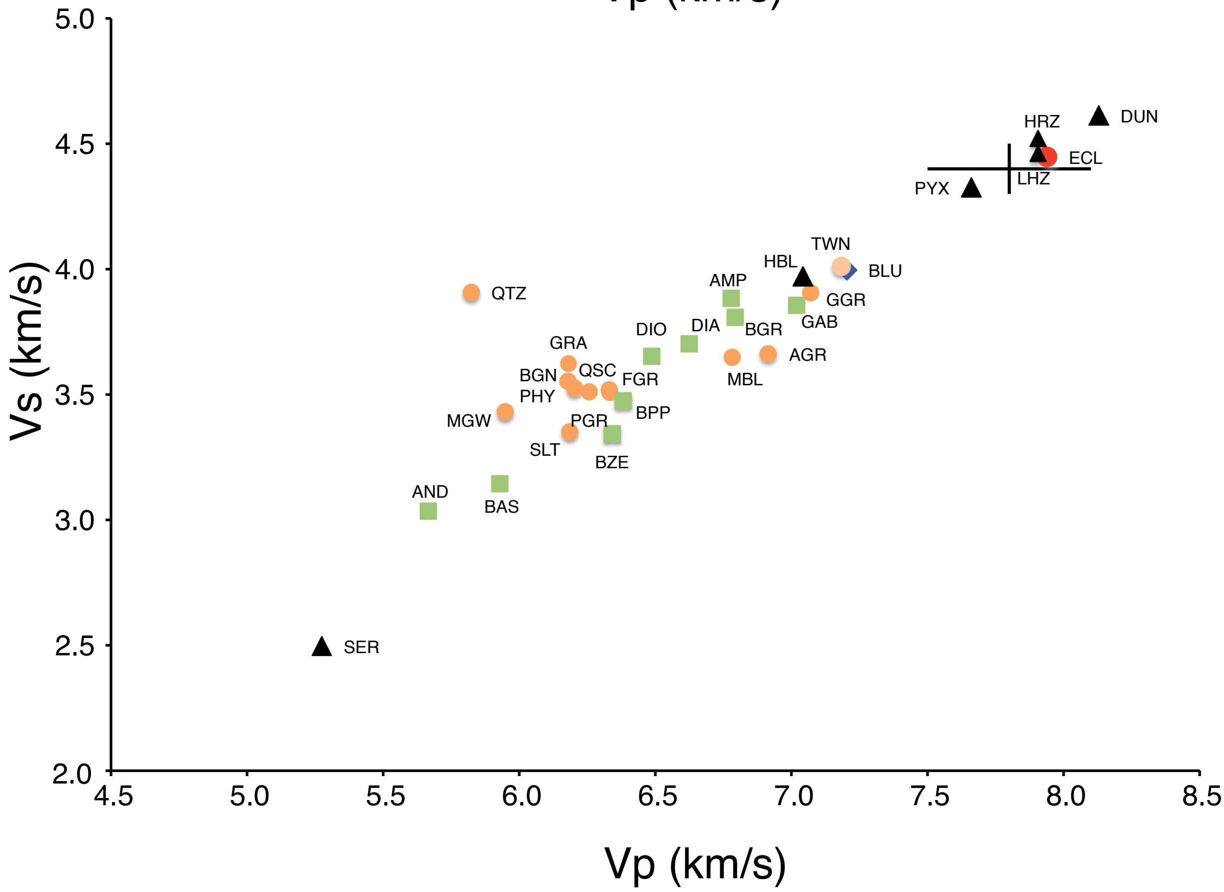

Figure S2. continued. Plots at 10 kilometer depth intervals. The Vp, Vs, and Vp/Vs range of interest at each depth interval is indicated by the black cross.

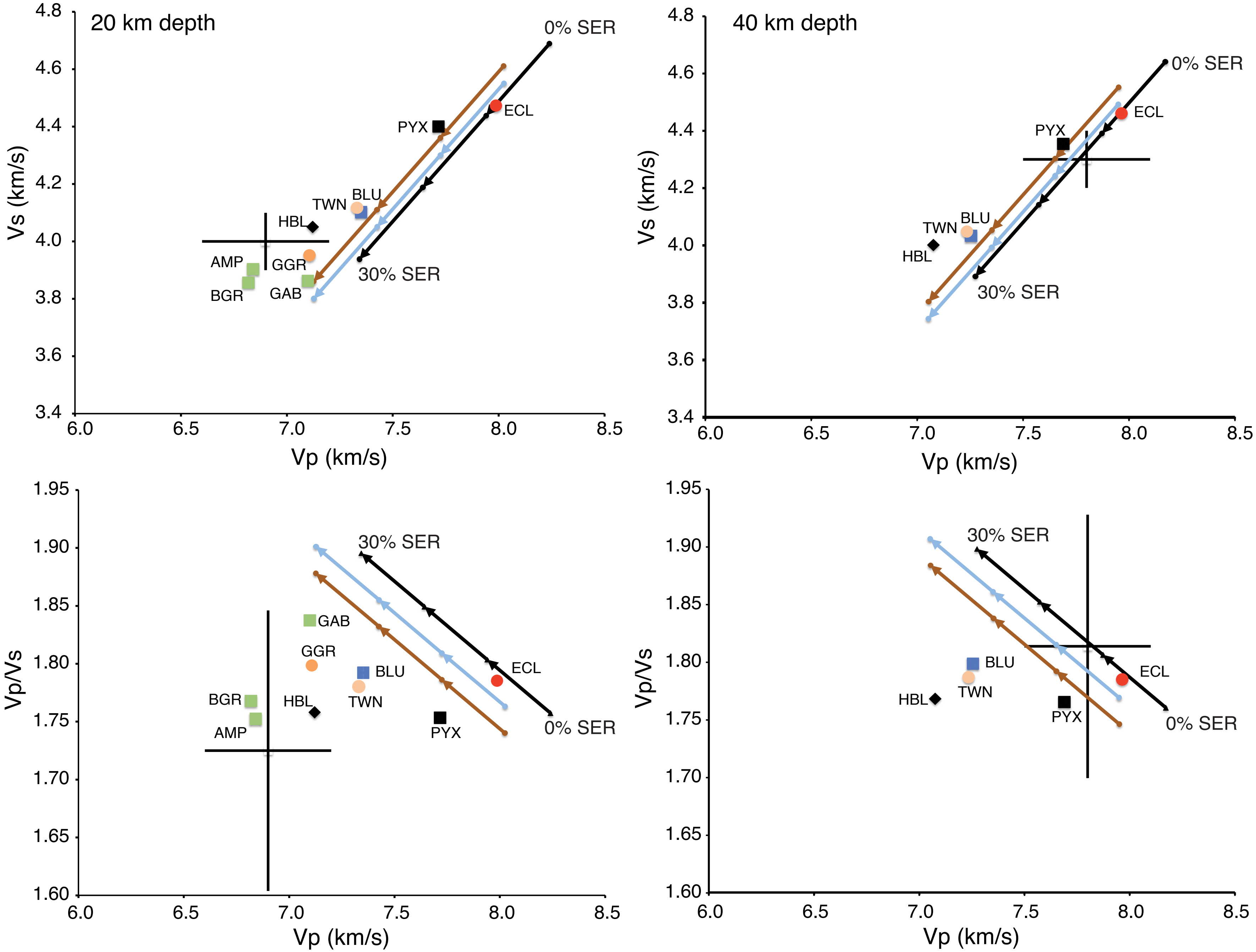

Figure S3. Vs vers Vp and Vp/Vs versus Vp plots of selected rocks of interest at 20 and 40 kilometers depth. The Vp, Vs, and Vp/Vs range of interest at each depth is indicated by the black cross. Labels are as in Figure 3.

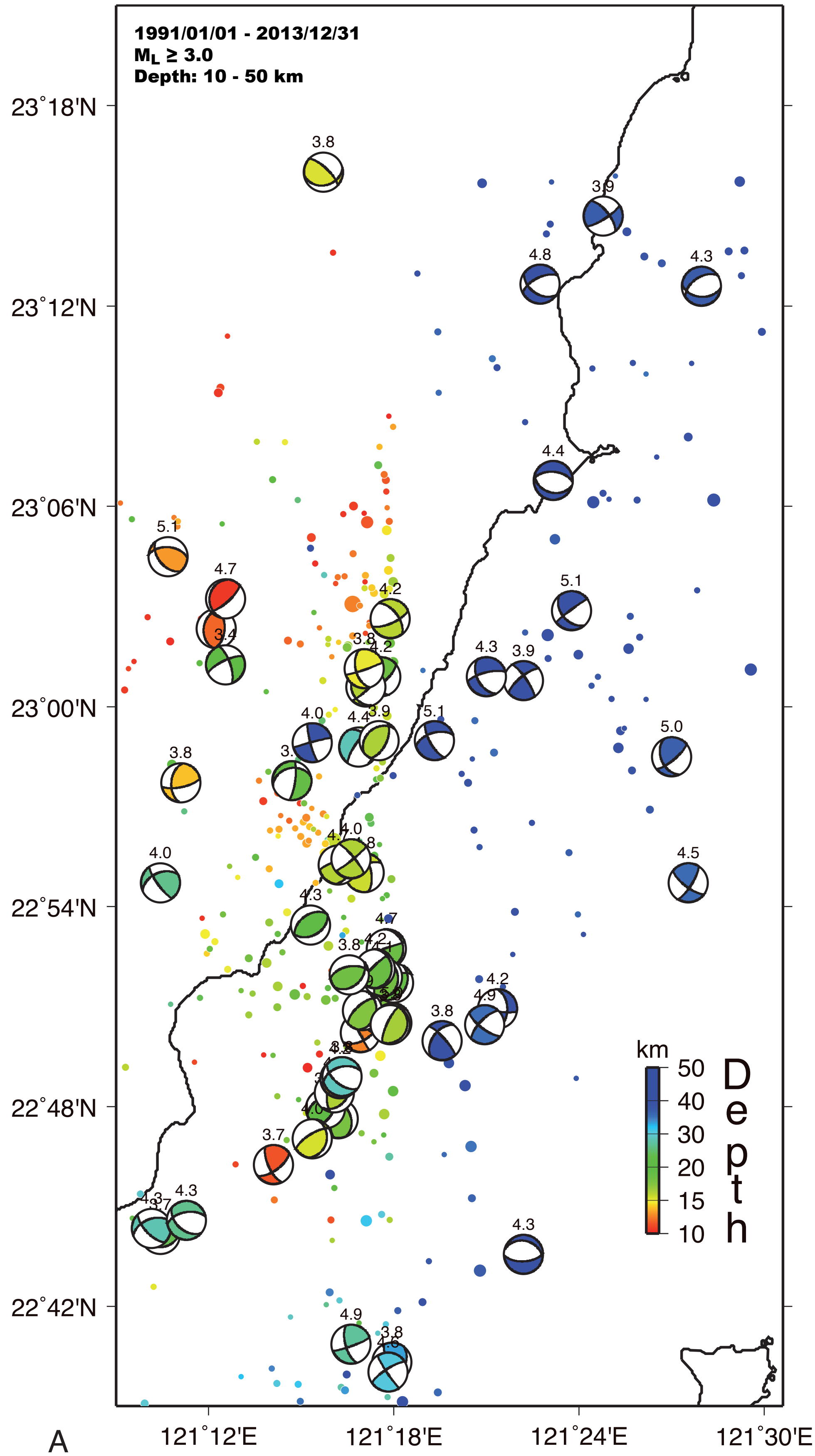

Figure S4. (a) Seismicity within the high-velocity zone and the 57 focal mechanisms determined. (b) Full waveform models of the 10 events shown in Figure 4.

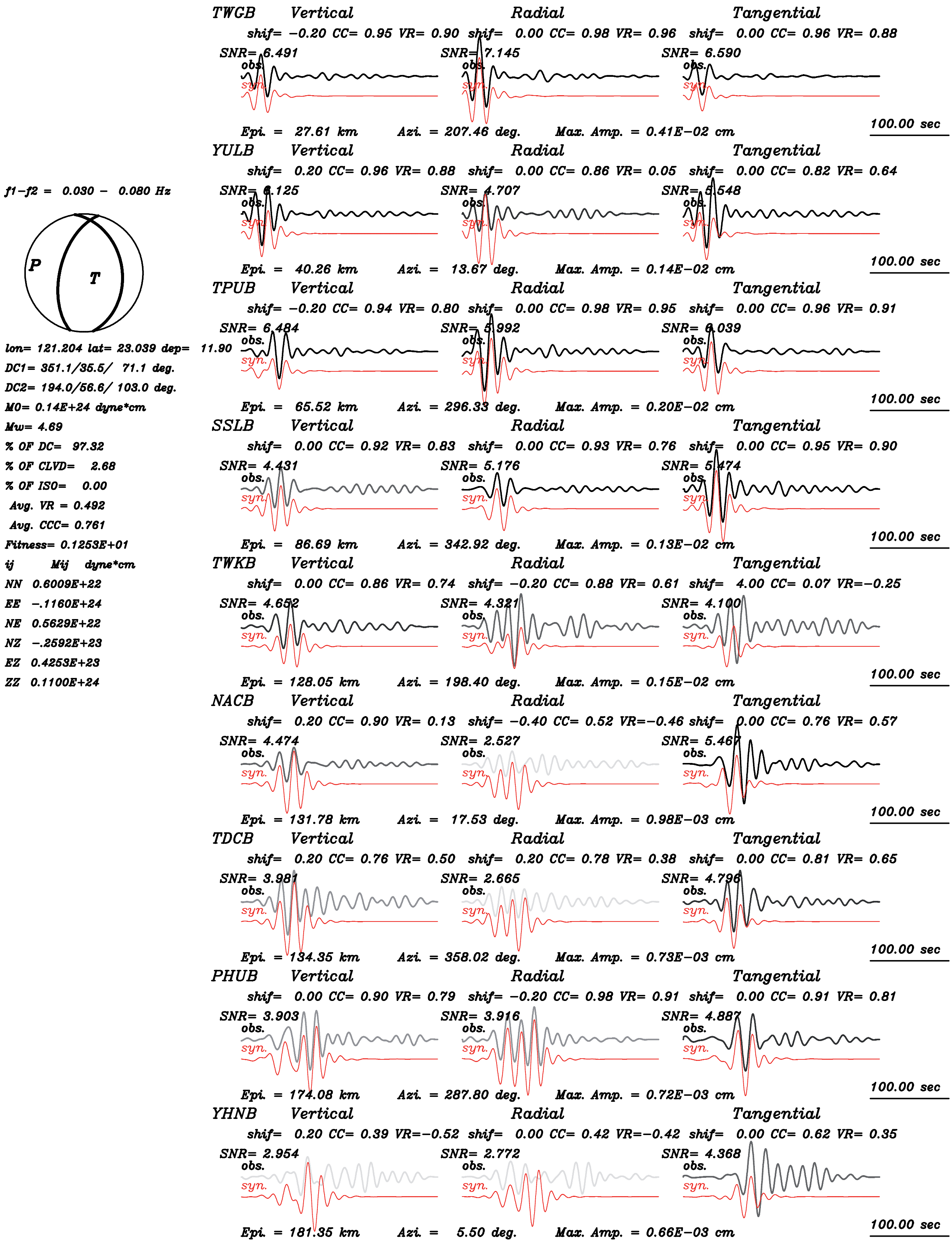

Figure S4. continued (b) Full waveform models of the events shown in Figure 4.

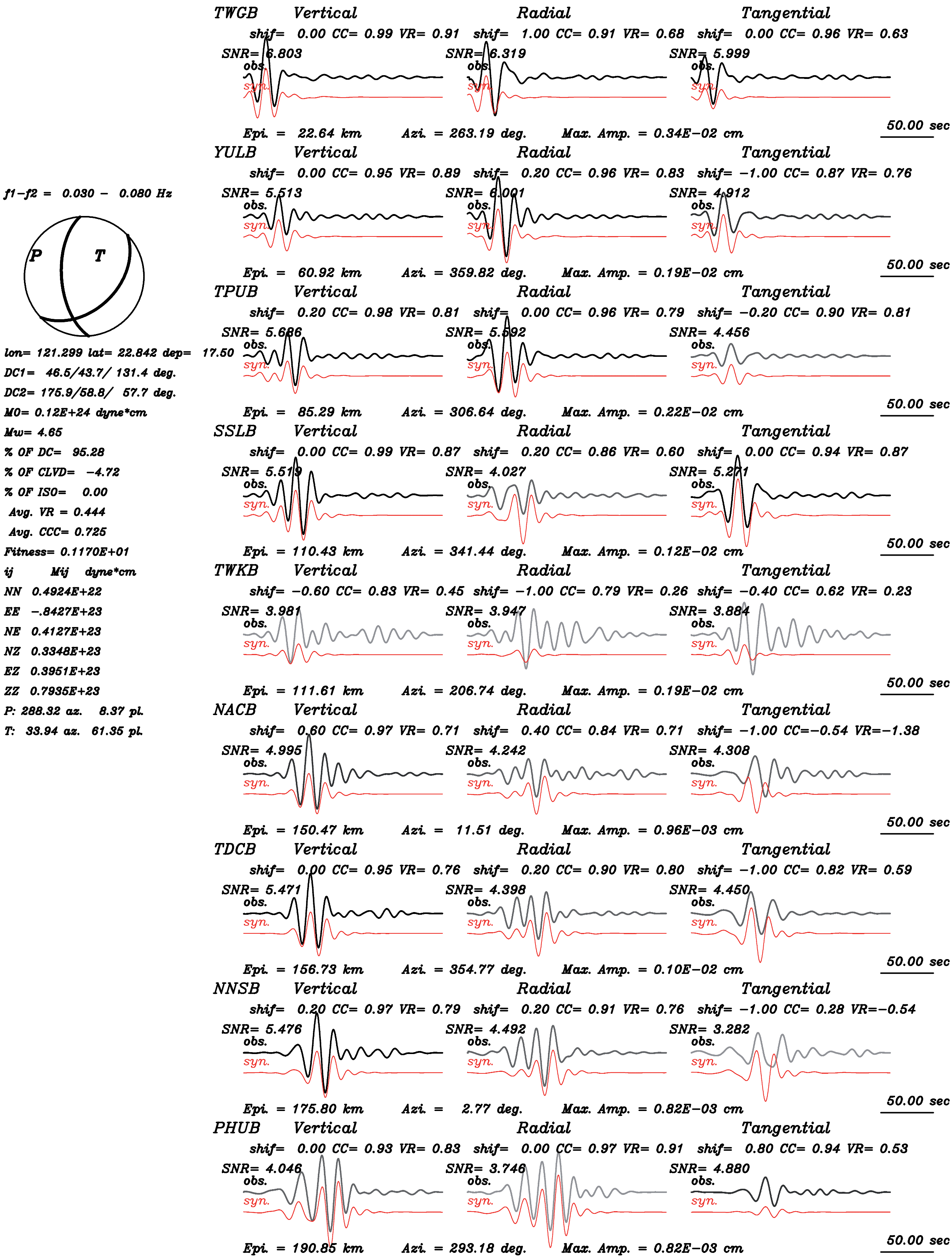

Figure S4. continued (b) Full waveform models of the events shown in Figure 4.

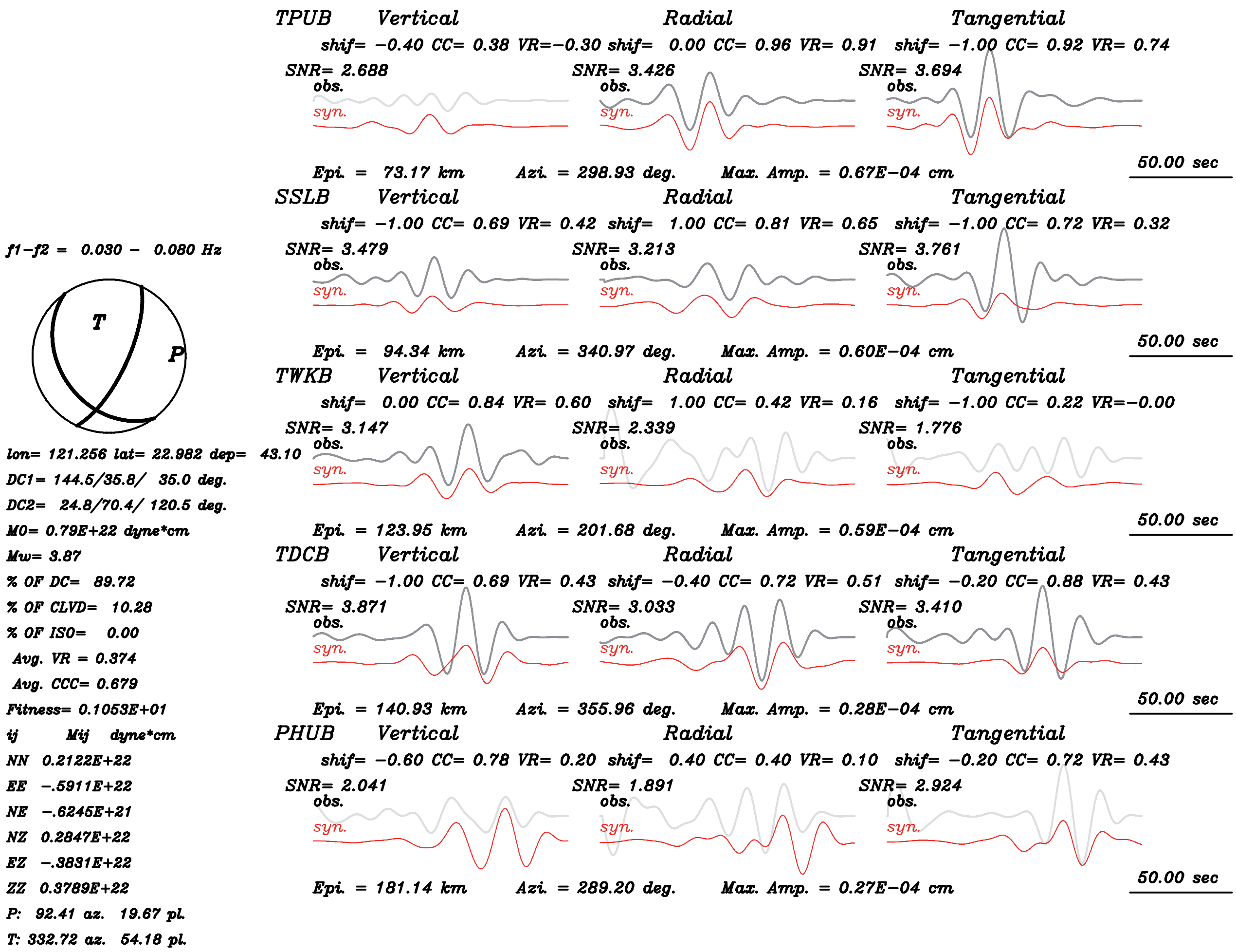

Figure S4. continued (b) Full waveform models of the events shown in Figure 4.

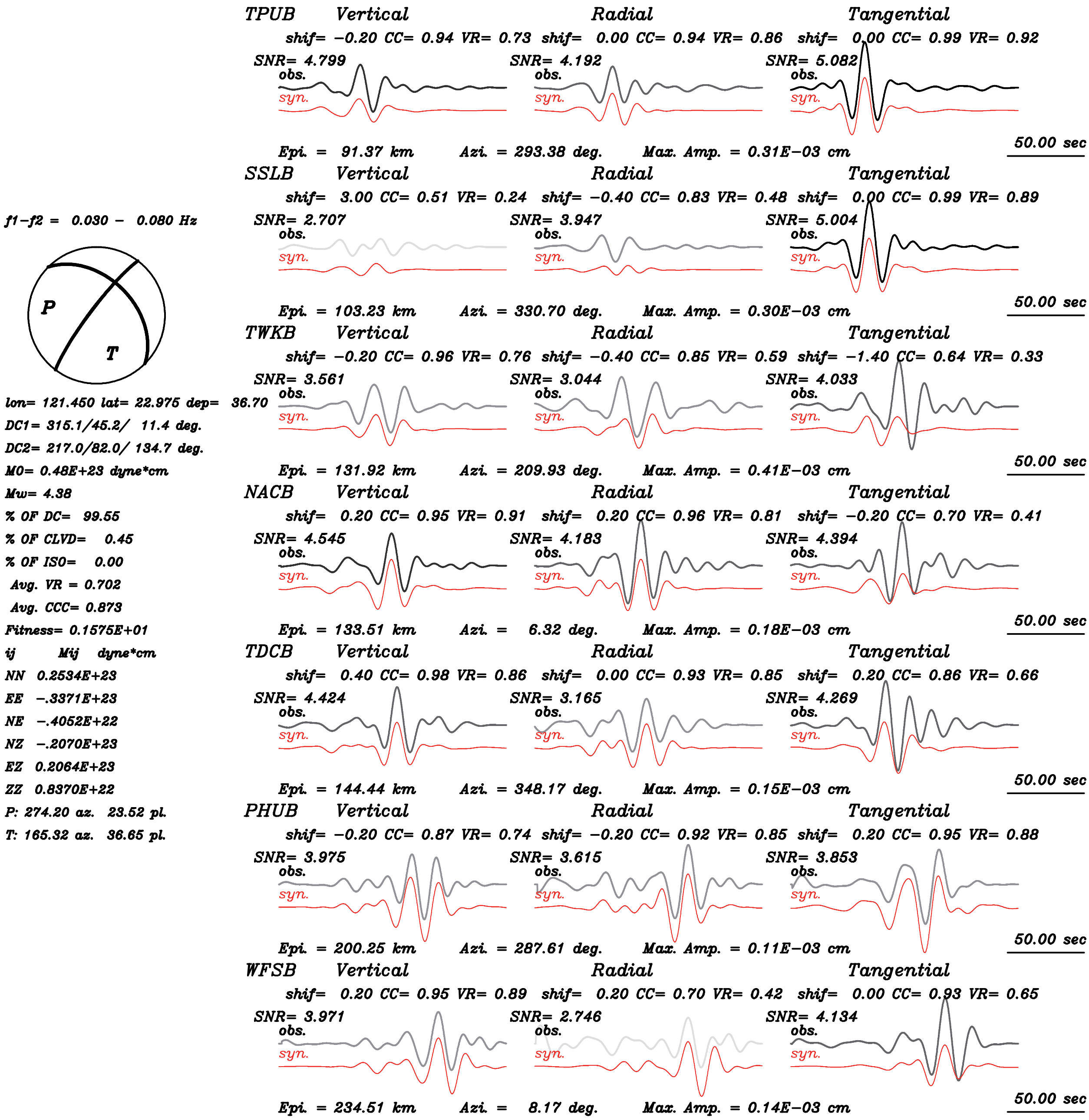

Figure S4. continued (b) Full waveform models of the events shown in Figure 4.

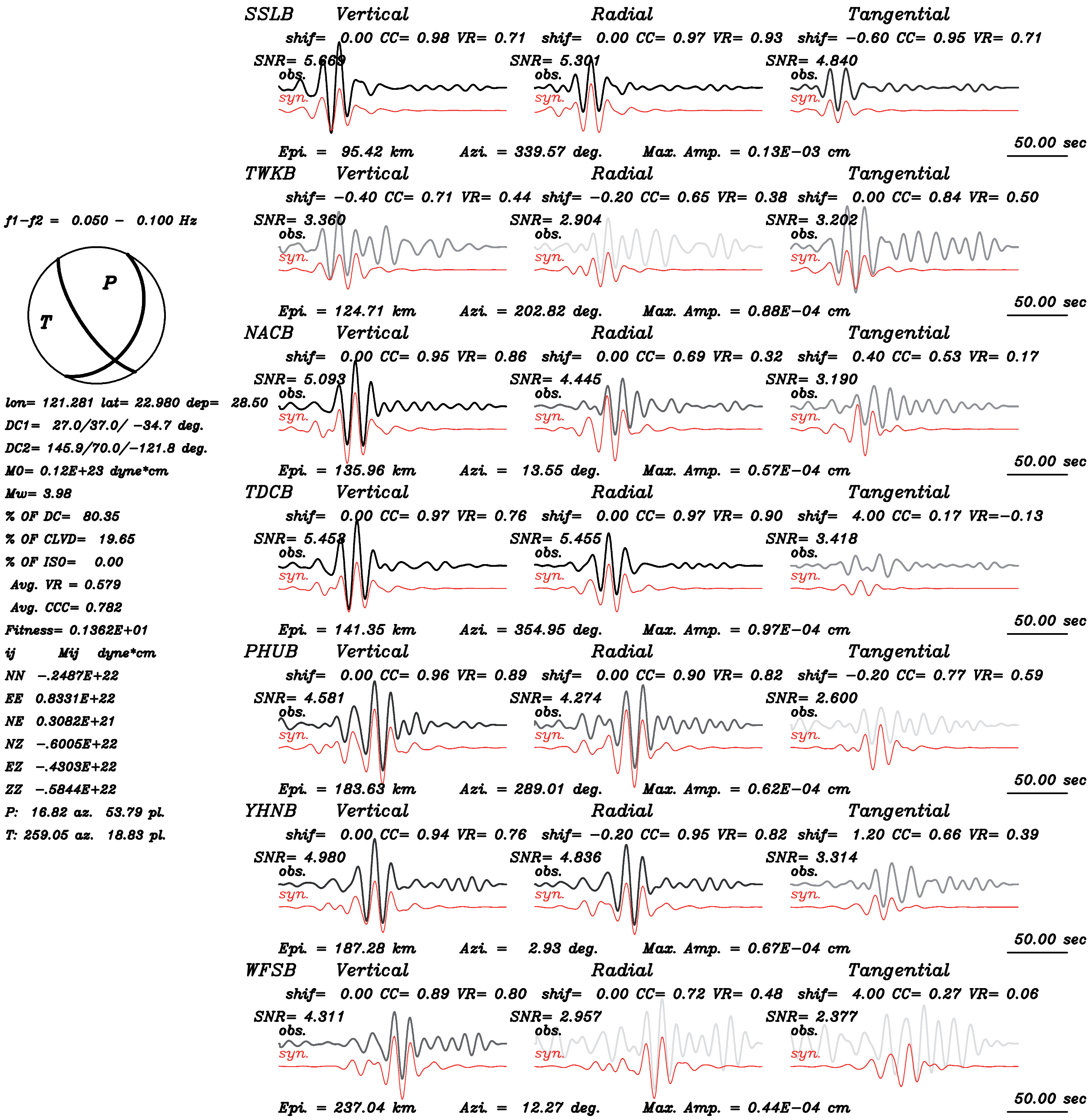

Figure S4. continued (b) Full waveform models of the events shown in Figure 4.

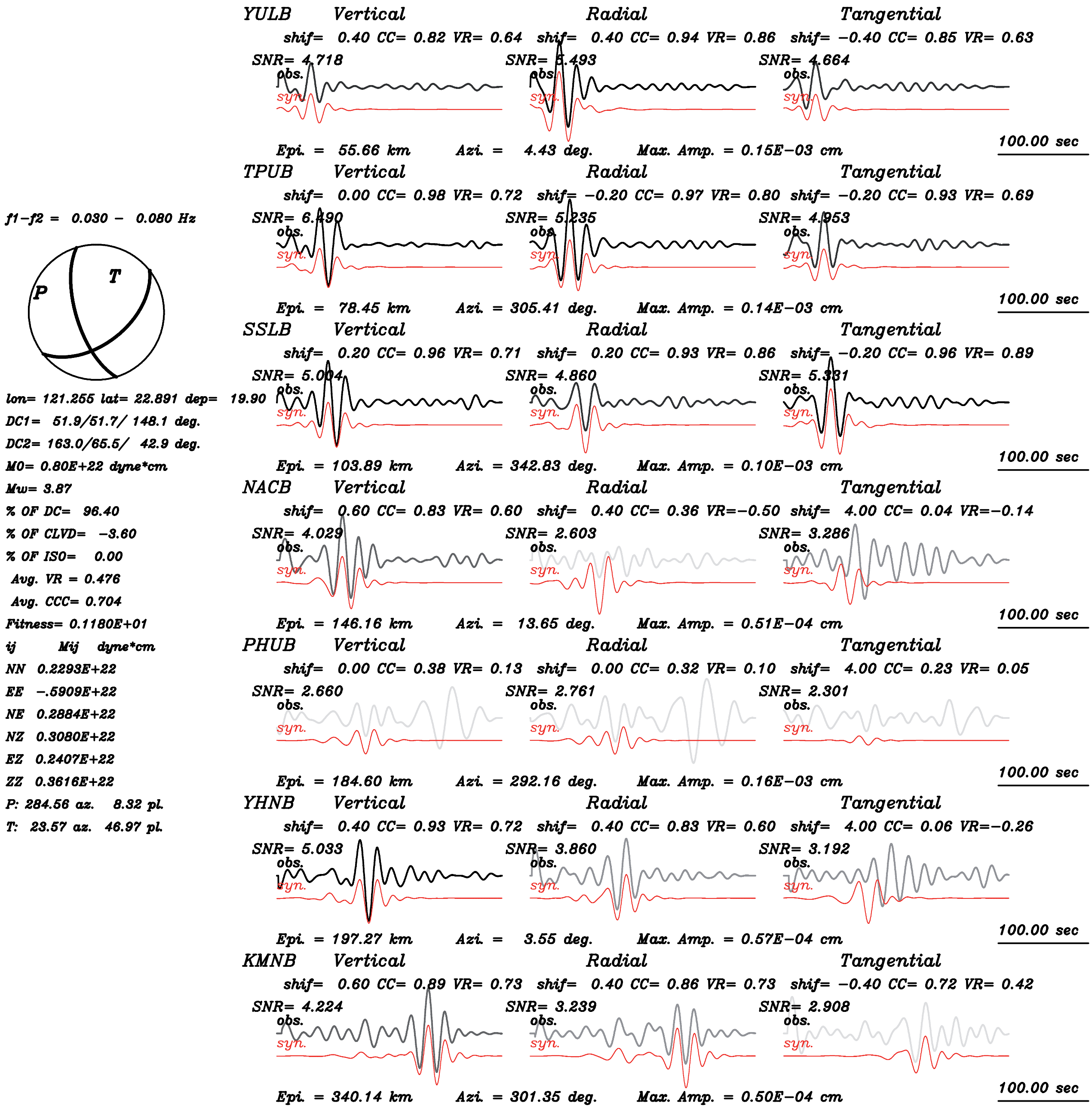

Figure S4. continued (b) Full waveform models of the events shown in Figure 4.

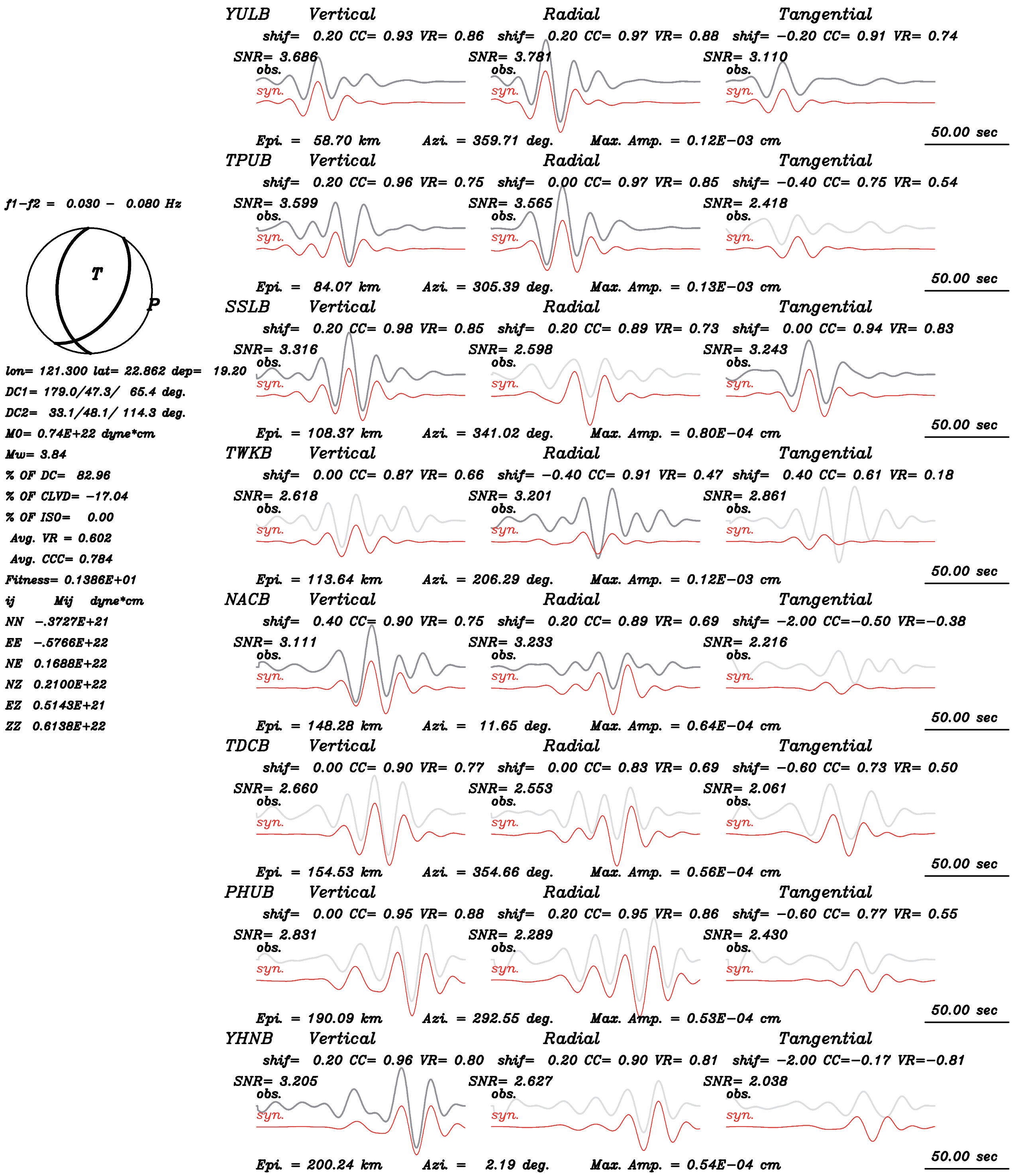

Figure S4. continued (b) Full waveform models of the events shown in Figure 4.

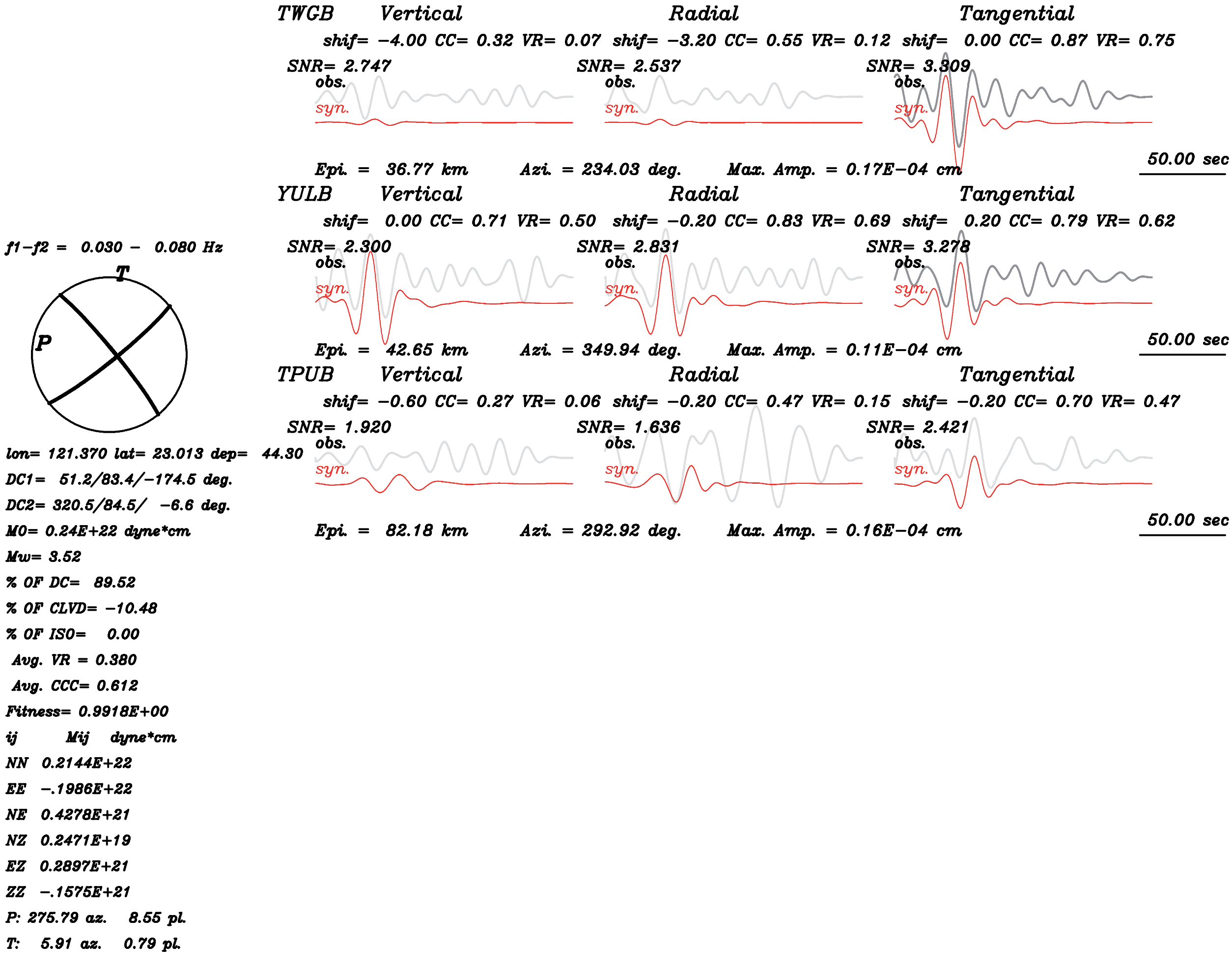

Figure S4. continued (b) Full waveform models of the events shown in Figure 4.

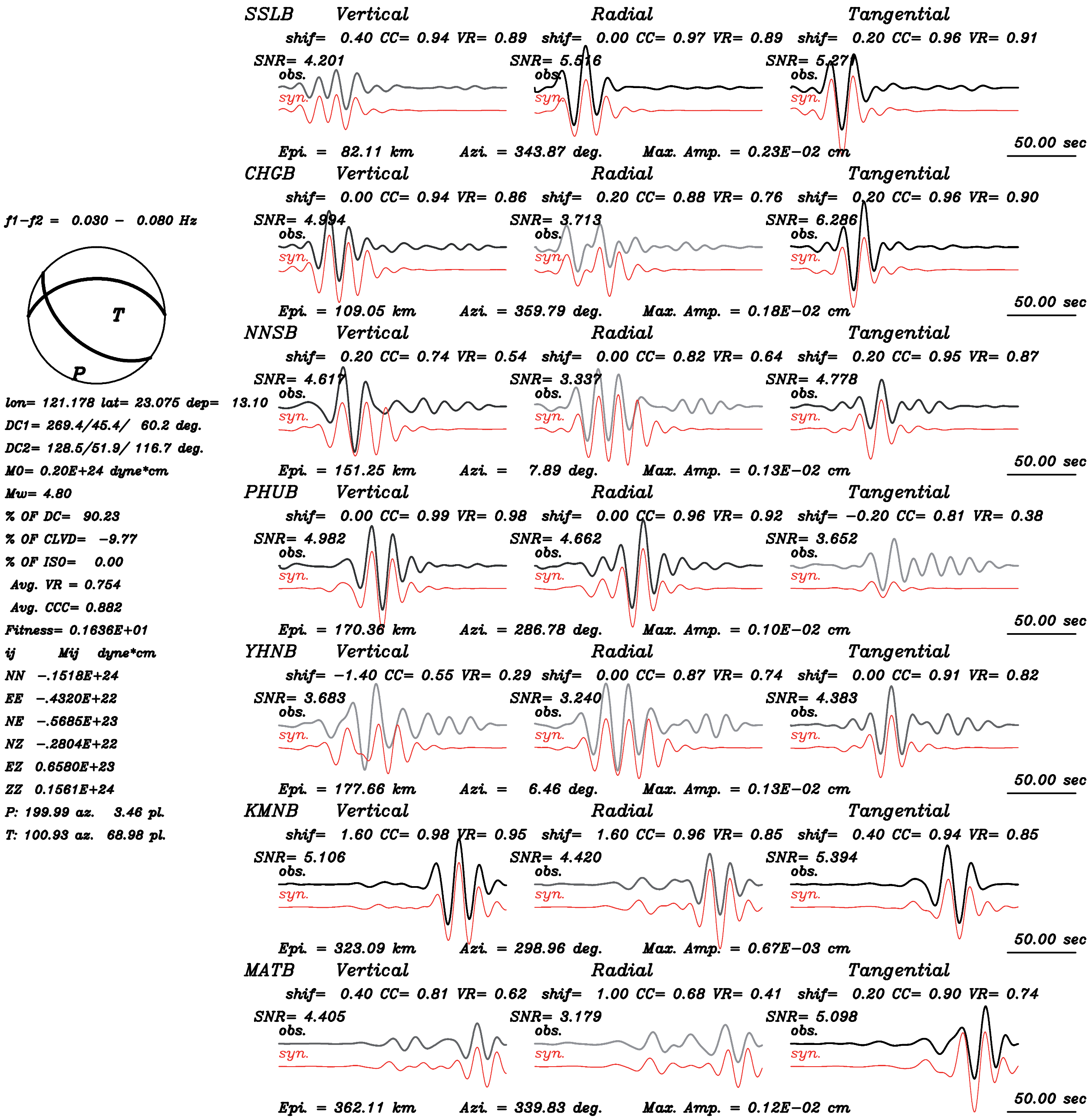

Figure S4. continued (b) Full waveform models of the events shown in Figure 4.

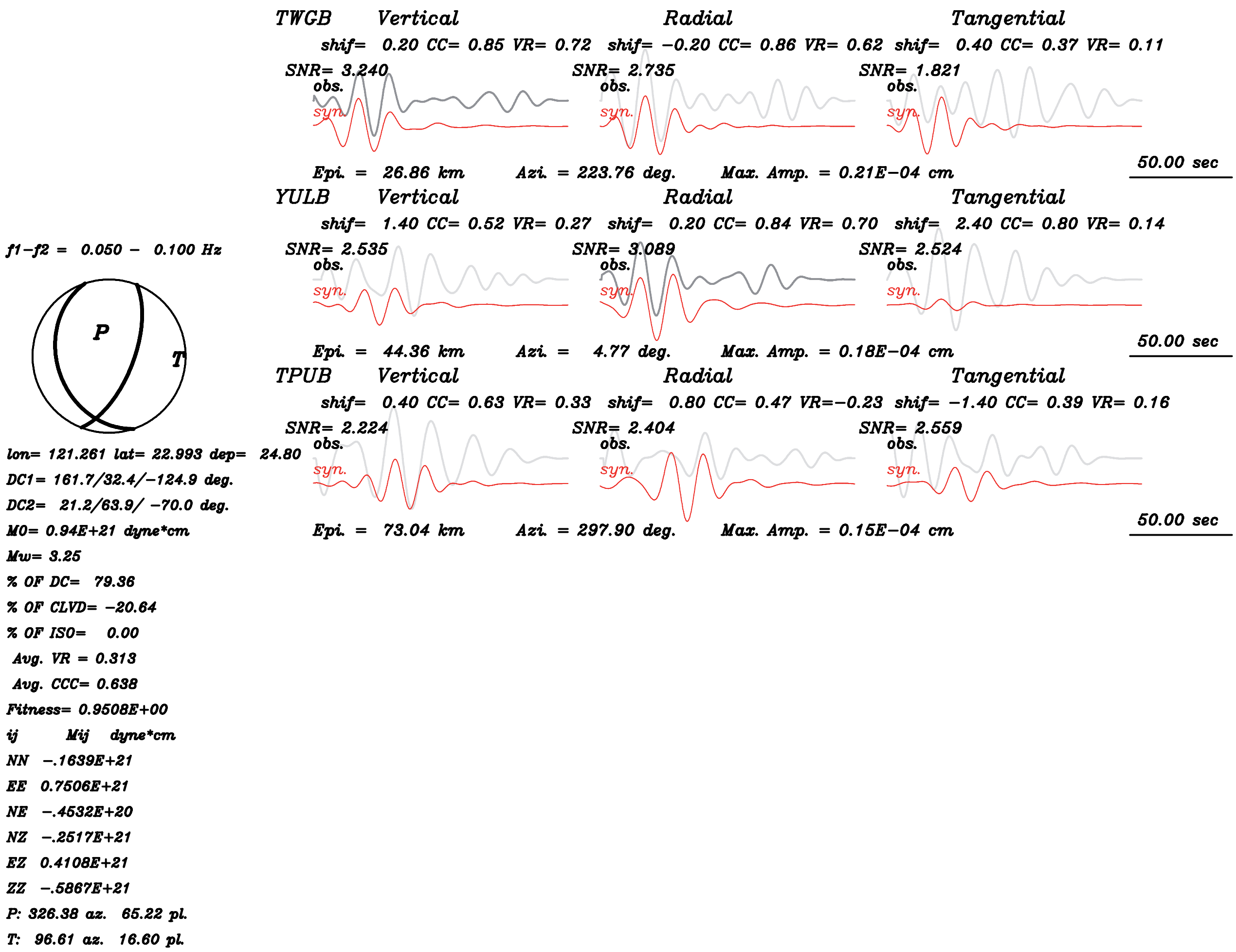

Figure S4. continued (b) Full waveform models of the events shown in Figure 4.